nature materials

Article

https://doi.org/10.1038/s41563-023-01660-8

Controlling liquid-liquid phase behaviour with an active fluid

Received: 16 July 2022

Accepted: 2 August 2023

Published online: 07 September 2023



Check for updates

Alexandra M. Tayar ¹□, Fernando Caballero ¹, Trevor Anderberg, Omar A. Saleh 10 1,2,3, M. Cristina Marchetti 1,3 & Zvonimir Dogic 10 1,3

Demixing binary liquids is a ubiquitous transition explained using a well-established thermodynamic formalism that requires the equality of intensive thermodynamics parameters across phase boundaries. Demixing transitions also occur when binary fluid mixtures are driven away from equilibrium, but predicting and designing such out-of-equilibrium transitions remains a challenge. Here we study the liquid-liquid phase separation of attractive DNA nanostars driven away from equilibrium using a microtubule-based active fluid. We find that activity lowers the critical temperature and narrows the range of coexistence concentrations, but only in the presence of mechanical bonds between the liquid droplets and reconfiguring active fluid. Similar behaviours are observed in numerical simulations, suggesting that the activity suppression of the critical point is a generic feature of active liquid-liquid phase separation. Our work describes a versatile platform for building soft active materials with feedback control and providing an insight into self-organization in cell biology.

Liquid-liquid phase separation (LLPS) is a pervasive phenomenon that plays a central role throughout physics, materials science, engineering, biology and everyday life¹⁻⁴. In equilibrium, the concentrations of the coexisting phases are controlled by thermodynamic parameters such as temperature and pressure. The input of mechanical energy influences the properties of LLPS. For example, shearing a two-phase system can modify the coexistence concentrations and suppress the critical point⁵⁻¹¹. Alternatively, systems can also be driven out of equilibrium not by the input of energy at macroscopic boundaries but by the continuous motion of energy-consuming microscopic constituents¹². Such internally driven systems exhibit diverse non-equilibrium dynamical states and phase transitions reminiscent of LLPS¹³⁻¹⁷. For example, even in the absence of attractive interactions, active Brownian particles undergo bulk phase separation into a dense liquid and a dilute gas¹⁸⁻²². In a different regime, increasing the motility of active particles with attractive interactions can suppress the phase separation and breakup dense condensate^{23,24}. These observations identify the activity as a promising parameter that controls phase behaviours and can be easily patterned in space and time²⁵. In active analogues of LLPS, such as Janus swimmers and motile bacteria, however, the same microscopic constituents generate the active forces and undergo phase separation. Generalizing these findings to a much wider range of passive materials exhibiting LLPS remains a challenge²⁶. Here we use activity to control the LLPS of a passive system composed of associative DNA nanostars²⁷. We merge this system with a microtubule (MT)-based active fluid exhibiting chaotic flows²⁸, finding that activity suppresses the critical-point temperature and narrows the concentration gap of the coexisting phases. The suppression of LLPS requires a direct mechanical link between the reconfiguring MT network and the passive entities undergoing the phase transition.

Coupling DNA-based droplets to an active fluid

Our experimental system had four main components. First, it contained associative multi-armed DNA nanostars with attractive hybridization interactions at the tip of their arms. DNA nanostars formed temperature-dependent dense liquid-like condensates that coexisted with a dilute gas phase (Fig. 1a and Supplementary Fig. 1) $^{27,29-31}$. The second

Department of Physics, University of California, Santa Barbara, CA, USA. 2Materials Department, University of California, Santa Barbara, CA, USA. ³Biomolecular Science and Engineering Program, University of California, Santa Barbara, CA, USA. 🖂 e-mail: Alexandra.tayar@weizmann.ac.il; zdogic@ucsb.edu

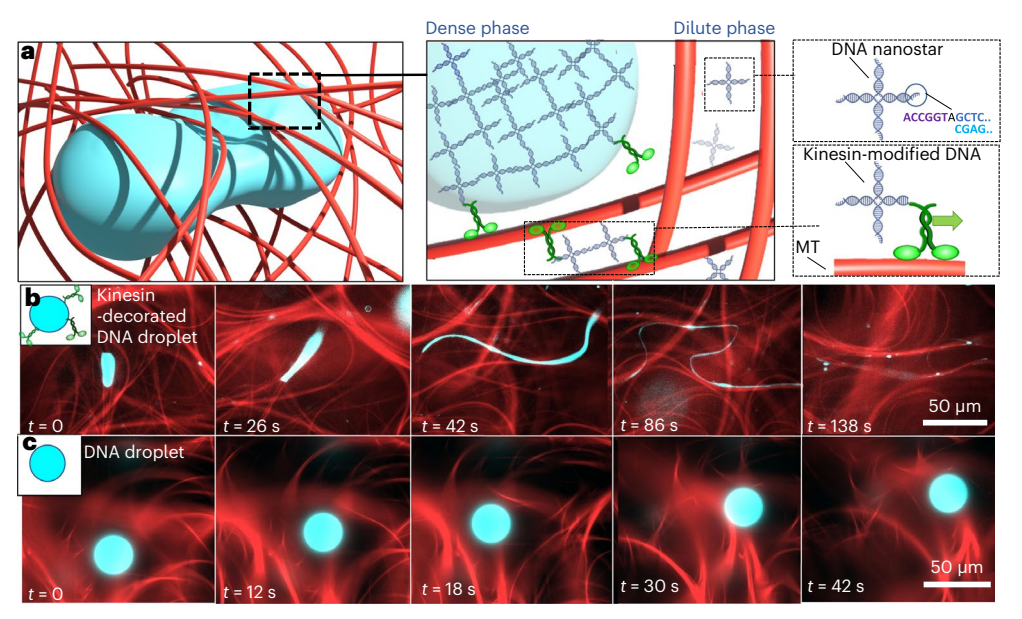


Fig. 1| **Active LLPS composed of DNA nanostars and MT-based active fluid. a**, DNA droplet enveloped by an active MT network. DNA nanostars phase separate into dense droplets and dilute gas, driven by the hybridization of a palindromic sequence at their tips. MTs partition into the dilute phase. Kinesin–DNAs have a motor attached to one arm, whereas the other three arms have attractive interactions. They bond droplets to MTs, and generate autonomous flows in

the dilute phase. **b**, DNA droplet (cyan) advected and deformed by the active MT network (red). **c**, Replacing kinesin–DNA with streptavidin-based clusters eliminates network–droplet coupling while preserving activity. The droplets are not considerably deformed but are advected by the active flows. The sample is in the steady state and t=0 indicates the beginning of the observed event. Kinesin–DNA concentration, 2.5 μ M.

component was the MT, micrometre-long filaments stabilized with non-hydrolysable nucleotide analogue GMPCPP. The third component was kinesin molecular motors covalently attached to one arm of DNA nanostars³². Kinesin-DNA had a dual purpose. When in the gas phase, they were bound to multiple MTs. Using energy from adenosine triphosphate (ATP) hydrolysis, they stepped along the MTs, powering interfilament sliding and generating chaotic active flows, similar to those previously studied²⁸. When displayed on the droplet surface, they provided a bond between the reconfiguring MT network and the DNA-based droplets. The network reconfiguration rate was determined by ATP concentration, which was kept constant using a biochemical regeneration system. The fourth component was the depletion agent poly(ethylene glycol) (PEG) (35 kDa, 2% w/v), which also had a twofold purpose. It induced attractive depletion interactions between the MTs³³, which increased the efficiency of motor clusters binding to multiple filaments—a feature essential for powering interfilament sliding and the generation of active stresses²⁸. The depletion agent can also promote the formation of DNA condensates³⁴. Importantly, besides kinesin-DNA and MTs, PEG and all the other components were present in both active mixtures and passive control samples (Methods). Thus, the role of PEG in shifting the phase diagram does not impact our comparisons. We observed that MTs exclusively partitioned into the dilute nanostar phase, rather than the condensate. This probably occurred because MTs repel DNA due to their mutual negative charge, and because MTs have a diameter of 20 nm that exceeds the nanostar condensate mesh size of 9 nm (refs. 29,31).

With decreasing temperature, passive DNA nanostars condensed into surface tension, minimizing the spherical droplets. The activity drastically deformed the spherical liquid droplets (Fig. 1b and Supplementary Video 1). In principle, these deformations could be driven by two interactions: short-ranged motor-mediated mechanical coupling of the reconfiguring MT network to the droplet or longer-ranged hydrodynamic flows. To determine the dominant interaction, we removed the kinesin–DNA, thus severing droplet–filament bonds and keeping the same DNA composition. In this case, the active flows were powered by orthogonal streptavidin–biotin kinesin clusters, the droplets were advected by the flow and they largely retained their

surface-tension-minimizing spherical shape (Fig. 1c and Supplementary Video 1). This suggested the essential role of network–droplet coupling. Simultaneously visualizing droplets and MTs provided additional evidence for the importance of such coupling (Fig. 1b). In particular, the deformation of mechanically coupled droplets followed the curvature of the MT bundles. The active flows, combined with the connectivity of the droplet to the cytoskeleton network, changed the droplet's surface area. After reaching a critical extension, the droplet disintegrated into smaller droplets.

Activity suppresses LLPS

The temperature-dependent equilibrium phase diagram of associative DNA nanostars can be described by a conventional Landau–Ginzburg free energy in terms of a scalar field representing the DNA concentration. Below a critical temperature of T_c = 24 °C, the system phase separated between the dilute nanostar phase and dense spherical droplets (Fig. 2a). At $T > T_c$, the dense droplets evaporated, generating a uniformly dispersed fluid phase. Next, we investigated how the activity influenced the phase behaviour for mechanically coupled droplets containing kinesin–DNA motors. At low temperatures (T < 19 °C), we observed continuously deforming droplets coexisting with a dilute gas (Fig. 2b and Supplementary Video 2). Above 19.5 ± 0.5 °C, the droplets evaporated. The difference in the critical-point temperatures between the two cases suggests that active stirring suppressed LLPS in DNA nanostars.

Next, we kept the temperature constant but varied the kinesin–DNA concentration, which controls the activity of the MT network and the network–droplet mechanical coupling (Fig. 2c). At low kinesin concentrations, active flows were slow, and droplets did not drastically deform (Fig. 2c–e). Increasing the kinesin–DNA concentration increased both flow speeds and droplet deformations and reconfigurations. Above 5.5 μ M kinesin–DNA concentration, the liquid–liquid coexistence disappeared, and we observed a uniform fluid phase. Temporal dynamics provided further evidence for the interplay between activity and LLPS. Active flows are powered by chemical energy from ATP hydrolysis. Once the kinesin motors depleted the ATP fuel, the non-equilibrium dynamics ceased, and the active fluid speeds dropped

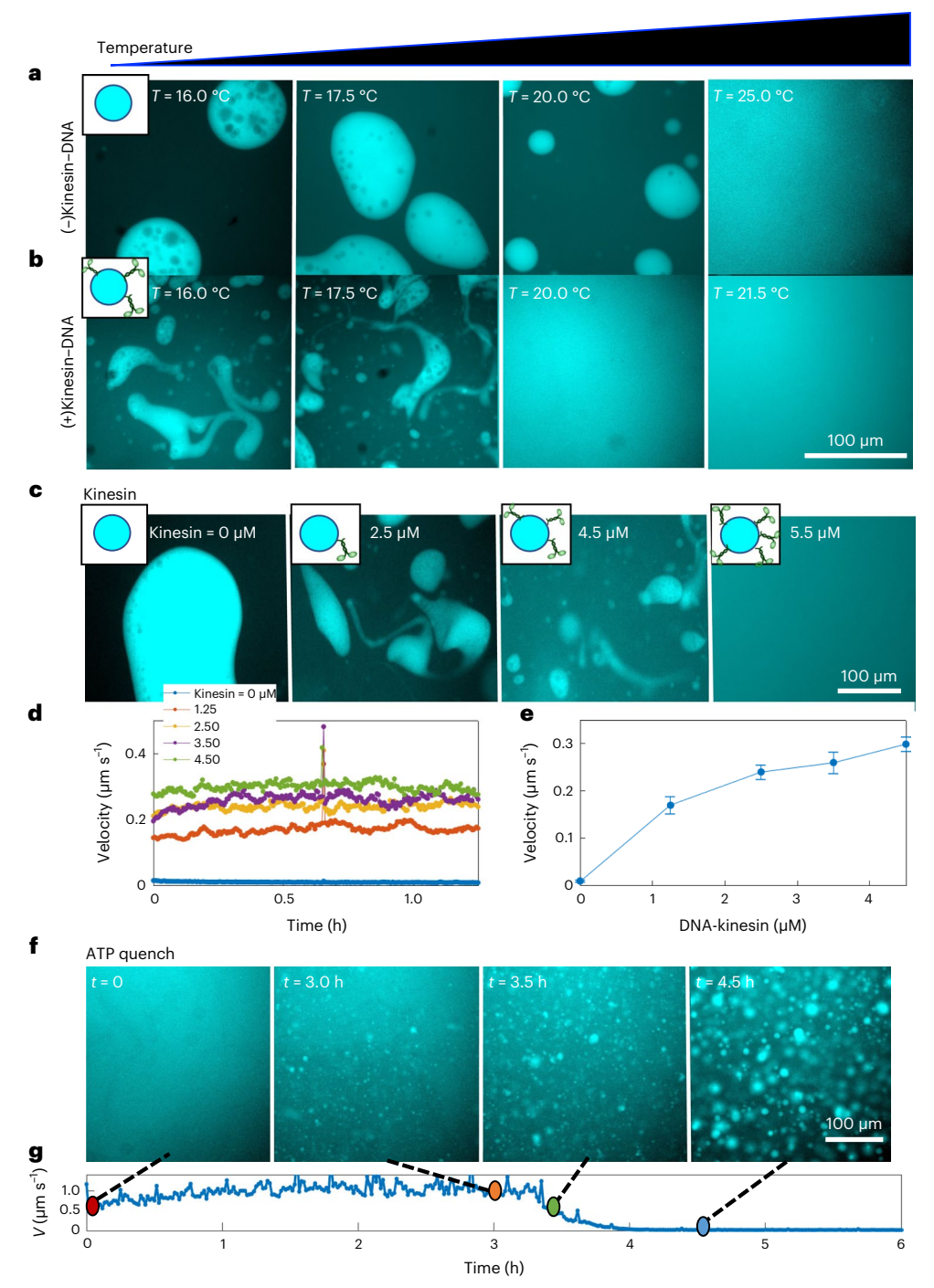


Fig. 2 | **Activity suppresses LLPS. a**, DNA droplets coexisting with an active fluid at different temperatures. The sample lacks kinesin–DNA, and activity is generated by streptavidin–kinesin motor clusters. **b**, DNA droplets coexisting with an active fluid in the presence of kinesin–DNA, which links MTs to droplets. Kinesin–DNA, 4.5 μ M. **c**, Increasing kinesin–DNA concentration increases both activity and network–droplet coupling. **d**, Steady-state flow speeds generated

at different kinesin–DNA concentrations; $T=18.5\,^{\circ}\text{C.}\,\mathbf{e}$, Active flow speeds as a function of kinesin–DNA concentration. Data points are the mean and standard deviation of the velocity averaged over 372 time points. \mathbf{f} , DNA droplets during an activity quench. Depleting ATP reduces the flow speeds, resulting in droplet nucleation, growth and coarsening. Kinesin–DNA, $4.5\,\mu\text{M.}\,\mathbf{g}$, Speed of active flows over the sample lifetime. In all panels DNA is at $4.5\,\text{mg}\,\text{ml}^{-1}(70\,\mu\text{M})$.

to zero (Fig. 2g). The decrease in the flow speeds was concomitant with the nucleation of new droplets and their subsequent growth (Fig. 2f, Supplementary Fig. 2 and Supplementary Video 3).

Measuring the influence of activity on phase diagram

Motivated by these observations, we measured the phase diagram as a function of both temperature and activity. DNA nanostar concentration

of the coexisting phases was estimated from the fluorescent intensities of the droplets and background, as well as the droplet area fraction (Supplementary Fig. 3). Imaging liquid–liquid coexistence at different temperatures revealed the equilibrium phase diagram of DNA nanostars, with a binodal curve that separated the two-phase and single-phase regime (Fig. 3(i)), similar to that found previously²⁷. Above a cloud temperature of $T_c = 23.5 \pm 0.3$ °C, there was only a uniform-density fluid phase.

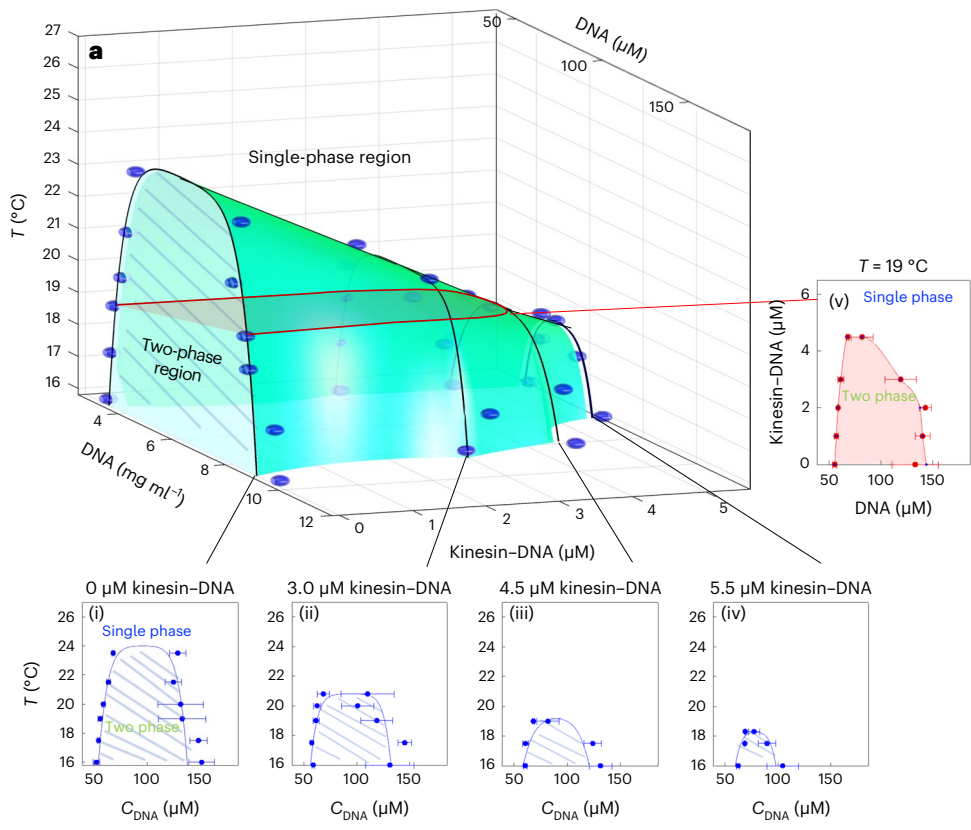


Fig. 3 | **Activity-dependent phase diagram of DNA nanostars. a**, LLPS phase diagram as a function of both temperature and activity, which is controlled by kinesin–DNA concentration. Two-dimensional cuts of the 3D phase diagram at different kinesin–DNA concentrations (C_{DNA}) ((i)–(iv)) and those at a fixed temperature and varying kinesin–DNA concentrations (v). Data points are the mean of 1,000 time points and averaged over $n = 3 \lor 4$ independent experiments.

The error bars are standard deviation of $n=3 \lor 4$ independent experiments. The black lines are guides for the eye. The surface is an interpolation between the black lines. The total DNA concentration before quench was 4.5 mg ml $^{-1}$ (70 μ M). All the samples have the same composition, except for the kinesin–DNA concentration.

To determine the influence of non-equilibrium driving, we measured the phase diagram in the presence of 5.5 µM kinesin-DNA (Fig. 3(iv)). The number of nanostar interacting arms influenced the shape of the phase diagram²⁷. To ensure a meaningful comparison, we only changed one parameter between the active and passive samples. Both had the same composition and a total DNA nanostar concentration of 65 µM, where 75% of the nanostars had four overhangs and 25% had three overhangs. To change the activity, we tuned the ratio of three-overhang nanostars with and without kinesin, and their total concentration was maintained constant. Activity generated by 5.5 µM kinesin-DNA changed the phase diagram in two ways. First, it lowered the cloud point temperature to 18.3 ± 0.3 °C. Second, it narrowed the concentration difference between the two coexisting phases. We repeated the same measurements for 3.0 and 4.5 μM kinesin-DNA (Fig. 3(ii), (iii), respectively). Combining these measurements uncovered a three-dimensional (3D) non-equilibrium LLPS phase diagram that is a function of both temperature and activity (Fig. 3a). We also measured the phase diagram at a constant temperature of 19 °C, and varied the kinesin-DNA concentration (Fig. 3(v)). Increasing the kinesin concentration reduced the width of the tielines. The system did not phase separate above a critical kinesin-DNA concentration, which was 4.5 μM. When interpreting these data, one should note that the kinesin stepping speed is temperature dependent; the average speed of the active fluid increased by 120% when changing the temperature from 19 to 23 °C (ref. 35).

Mechanically coupled droplets were composed of three distinct elements: (1) DNA nanostars with four interacting arms, (2) benzylguanine (BG)-modified DNA nanostars with three overhangs and (3) kinesin

motors attached to BG-modified DNA nanostars at varying concentrations (0–5.5 μ M). Different DNA components could, in principle, partition differently between the two phases. For example, driven by their affinity for MTs, the kinesin–DNA could preferentially partition into the MT-rich nanostar gas phase. At the same time, four-overhang nanostars could be enriched in the dense droplets. To check for these possibilities, we labelled the three DNA-based components and determined their partitioning between the two phases. We found that all components were homogeneously distributed within the droplet (Supplementary Fig. 4a,b). Furthermore, all components similarly partitioned between the dilute and dense phases (Supplementary Fig. 4c,d). Thus, the total DNA concentration axis of the 3D phase diagram describes the partition of all DNA-based components (Fig. 3).

In the dilute phase, nanostars could be monomeric or oligomerized due to their attractive ends. To characterize the possible structures, we used fluorescence correlation spectroscopy, a sensitive probe of the nanostar cluster size. Such an analysis revealed that the nanostars in the dilute phase were either monomeric or dimeric, and there was no discernible signal of larger-sized clusters (Supplementary Fig. 5). Note that interfilament sliding requires motor clustering, and this activity might be generated by the DNA dimer population that can link multiple motors.

Coupling between the active fluid and liquid droplets

The activity-induced suppression of LLPS requires motor-mediated mechanical coupling between the droplets and MT network. To

demonstrate this, we removed kinesin-DNA and generated activity using streptavidin-kinesin clusters that drove active flows but eliminated MT-droplet mechanical coupling (Fig. 4)²⁸. Increasing the streptavidin-kinesin cluster concentration increased the active flows from 0 to 8 µm s⁻¹, up to 20-fold faster than the velocities generated at the highest kinesin-DNA concentrations we studied. In the absence of mechanical coupling, the droplets remained circular at low velocities, whereas for higher velocities, they started deforming. However, increasing the velocity in this system did not alter the coexistence concentrations. Next, we kept the DNA concentration constant and changed the temperature. Again, there was no measurable difference between an equilibrium system and one driven by active flows but lacking MT-droplet coupling (Supplementary Fig. 6). Adding 3 µM of kinesin-DNA introduced mechanical droplet-filament coupling and minimally altered the speed of autonomous flows. In this case, coexistence concentrations narrowed with increasing flow speed and a critical point appeared.

The non-equilibrium phase diagram demonstrates the essential role of motor-mediated MT-droplet coupling. To gain a molecular insight, we simultaneously visualized the 3D MT network structure and the droplet shape. A projection reveals the structure of the MT network located up to 5.5 µm from the droplet surface (Fig. 5a and Supplementary Video 4). Droplets lacking kinesin–DNA components remained predominantly spherical, with MT bundles only intermittently contacting their surface. The bundles did not generate coherent flows at the surface. In comparison, the presence of the kinesin-DNA link qualitatively changed the network-droplet interactions. Specifically, such droplets exhibited large shape distortions and spontaneous breakups (Fig. 5b and Supplementary Video 5). Such deformations were driven by MT bundles that remain connected to the droplet surface over an extended time. Intriguingly, the droplet breakup was driven by the MT alignment. The extensile motion of surface-bound MTs generated a narrow neck that eventually ruptured, creating two daughter droplets (Fig. 5b).

We quantified how the deformations generated on the droplet's surface propagated into the interior. Using particle tracking velocimetry of MTs and bead-doped samples, we measured the velocity field both outside and within the droplets (Supplementary Video 6). We extracted the eigenvalues of the simple shear rate, denoting the local deformation of each fluid element invariant to the coordinate system. The magnitude of the simple shear rate averaged over different contours as a function of distance from the droplet surface revealed how deformations propagate across the interfacial boundaries (Fig. 5c and Supplementary Video 6). Droplets lacking kinesin–DNA showed a profile quickly decaying to zero in the droplet interior, whereas kinesin-decorated droplets had a non-zero shear rate in the droplet.

Continuum theory of LLPS of active fluids

Previous efforts studied LLPS in active fluids of spherical particles. Such systems are described with the Cahn-Hillard theory that couples the dynamics of a scalar field ϕ describing the concentration of one of the species to the flow field v. These scalar models predict negative interfacial tension and arrested phase separation^{36,37}. However, they fail to predict the suppression of critical temperature observed in our experiments. This is not entirely surprising as our active fluid is composed of anisotropic MTs that can acquire local orientational order, whereas previous models studied active fluids with spherical constituents. The non-equilibrium dynamics and the associated flow of active liquid crystals composed of anisotropic particles are very different from those formed by spherical particles¹². Specifically, active liquid crystals exhibit a ubiquitous bend instability, which, in turn, drives turbulent-like chaotic flows. Previous work has shown that the MT-based 3D active fluid used in our experiments is well described by a coarse-grained hydrodynamic theory of active liquid crystals38,39.

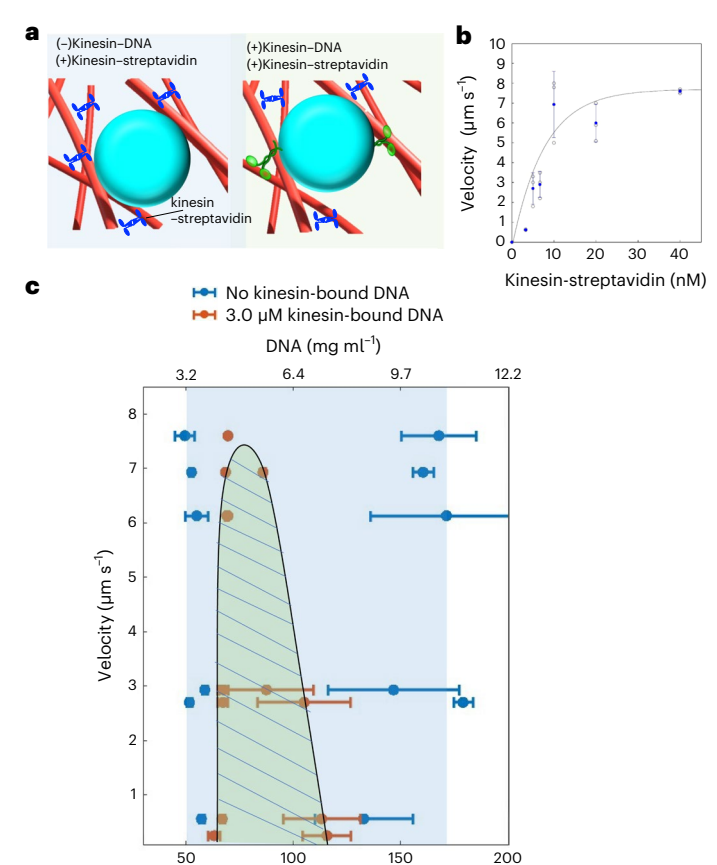


Fig. 4 | **LLPS suppression requires MT–droplet interactions. a**, Illustration of a system lacking kinesin–DNA (blue) and for a system where MT–droplet interactions are mediated by kinesin–DNA. **b**, Background velocity as a function of the concentration of streptavidin–kinesin motor clusters. **c**, Phase diagram as a function of the flow velocity for a system lacking kinesin–DNA (blue) and for a system where MT–droplet interactions are mediated by 3 μ M kinesin–DNA. Velocity of autonomous flows is controlled by streptavidin–kinesin clusters that drive active flows but do not couple droplets to MTs. The values represent mean and standard deviation for 1,000 time points, with $n=3 \lor 4$ independent experiments. Lines are a guide to the eye.

DNA (µM)

Motivated by the above consideration, we explore the role of turbulent flows generated by the coupling of activity to orientational order in controlling the LLPS. In particular, we couple the dynamics of DNA concentration ϕ and flow field \mathbf{v} to the nematic order parameter Q_{ii} describing the orientational order of the active fluid. Similar models have been used before to describe active/passive interfaces 40-42, but the influence of activity on the phase diagram has not been studied. The concentration field ϕ is advected by flow and phase separates according to the Cahn–Hilliard dynamics, $D_t \phi = \nabla^2 \left(\frac{\delta F_{\phi}}{\delta \phi} \right)$, where $D_t = \partial_t + \mathbf{v} \cdot \nabla$ and $F_{\phi} = \frac{1}{2} \int \frac{1}{2} \left[(\phi^2 + a)^2 + \kappa (\nabla \phi)^2 \right]$, into DNA-poor $(\phi_- = -\sqrt{-a/2})$ and DNA-rich $(\phi_+ = +\sqrt{-a/2})$ phases when a < 0(Fig. 6a,b). Here $a \propto (T - T_c)/T_c$ plays the role of reduced temperature. In equilibrium, the critical point is $a_c = 0$ for a symmetric mixture $(\phi_0 = \frac{1}{r} \int_V d^2r \phi(r, 0) = 0)$ and the coexistence line is the inverted parabola, that is, $a = -\phi_0^2$ (Fig. 6c). The Q tensor relaxes at a rate controlled by the nematic free energy F_Q that incorporates the elasticity of the liquid crystal and is stirred by the strain rate D_{ij} and vorticity ω_{ik} , with $D_tQ_{ij}=\lambda D_{ij}+Q_{ik}\omega_{kj}-\omega_{ik}Q_{kj}+\frac{1}{\gamma}\frac{\delta F_Q}{\delta Q_{ij}}$ (ref. 12). The flow is described by the Navier–Stokes equation $\rho D_t \mathbf{v}=\nabla \cdot \boldsymbol{\eta}(\boldsymbol{\phi})\nabla \mathbf{v}-\nabla P+\mathbf{f}$, with force

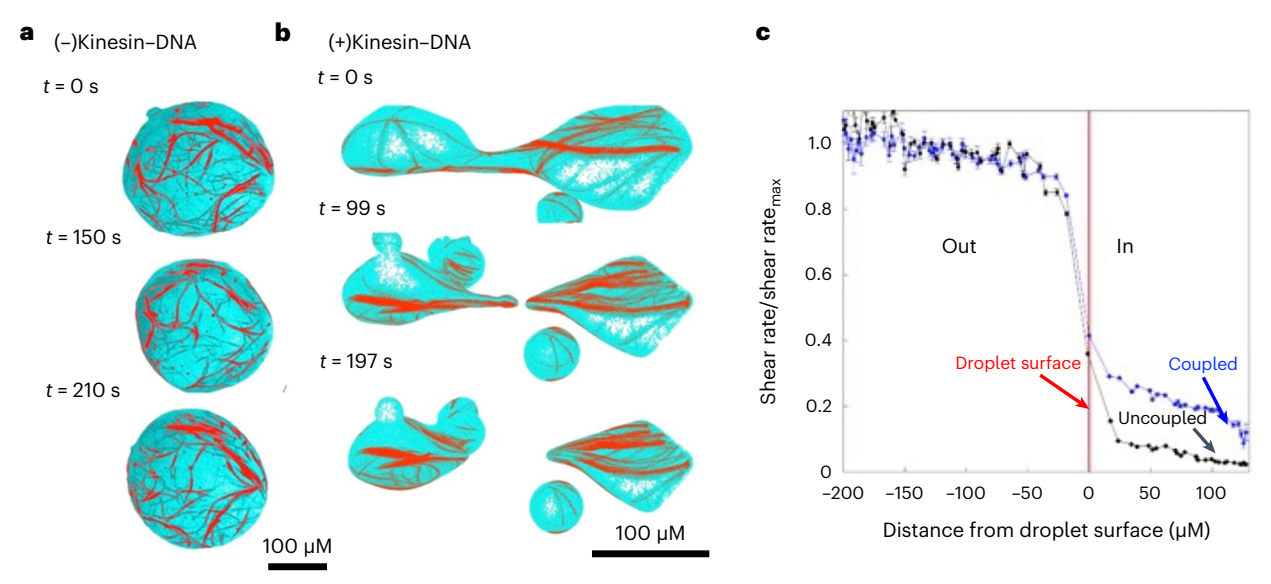


Fig. 5 | **MT network couples to DNA droplets. a**, MT-droplet interactions in a system lacking kinesin–DNA. The droplet is shown in cyan. The MTs within $11 \, \mu m$ of the droplet surface are shown. **b**, Coupling between DNA droplets and MT network in the presence of kinesin–DNA. MTs within $5.5 \, \mu m$ of the droplet

surface are shown in red. c, Normalized simple shear-rate dependence of the distance from the droplet interface. Each point is binned over 400 time points and averaged over three samples. The error bars are the size of the data points or smaller. Kinesin–DNA, 3 μ M.

 $f_i = f_i^{\phi} + f_i^a$ comprising passive capillary forces f_i^{ϕ} and active forces $f_i^a = \partial_j \left(\alpha(\phi)Q_{ij}\right)$; here $\alpha(\phi)$ is an active stress that vanishes in the passive, DNA-rich fluid and has a constant value of $\alpha_0 < 0$ in the active, DNA-poor phase (Supplementary Information). The dilute and dense phases have different viscosities η . We use a single velocity field that continuously varies across the fluid–fluid interface, which accounts for the mechanical coupling of MTs to liquid droplets (Fig. 6d). This assumption is supported by the experimental observations that shear flows generated in the active-fluid phase propagate into the droplet interior, as evident in the experiments (Supplementary Fig. 7).

We numerically solved our model to obtain the phase diagram as a function of effective temperature (a) and activity (α). The calculated phase diagram captures the main experimental features, namely, the shift in the critical point to lower temperatures and the narrowing of the coexistence region (Fig. 6c). Furthermore, in the coexistence region, the phase separation dynamics are arrested and one observes a dynamical steady state consisting of finite-sized droplets (Fig. 6a and Supplementary Video 7). Our model leads to an understanding of how active fluids control the phase diagram of equilibrium LLPS. To capture the observed behaviour, the active force, $f_i^a = f_i^{a,b} + f_i^{a,s} = \alpha(\phi)\partial_i Q_{ii} + Q_{ii}\partial_i \alpha(\phi)$, has to have both bulk and interfacial contributions arising from activity gradients. Extensile $(\alpha < 0)$ interfacial stresses shear the interface, favouring their formation and breakup into a bulk-phase-separated system. Simultaneously, flows generated by the bulk active stresses throughout the active phase are essential for shifting the critical point and narrowing the coexistence region^{12,43,44}. Approach to the critical point is associated with the critical slowing down, as well as the growth of the lifetime of critical fluctuations in the homogeneous state. This unbounded growth is restricted by active stirring that injects energy into the system at a rate $|\alpha|/\eta$. Consequently, the critical point is suppressed once the active shear rate overcomes the rate at which the gradients spontaneously develop. This mechanism is analogous to a critical fluid subjected to external shear, where one also finds the suppression of the critical point when the externally imposed shear rate exceeds the rate of passive relaxation⁶. We emphasize that the role of activity on phase separation has been studied before in the context of scalar models where activity enters in the form of non-equilibrium capillary forces that break detailed balance^{36,37,45}. In this case, the activity can arrest phase separation, but does not affect the location of the critical point and size of the coexistence region. We, therefore, conclude that the coupling to liquid-crystalline degrees of freedom is the key for experimentally observed suppression of phase separation.

Several comments are pertinent when comparing our model with experiments. First, in principle, nanostar-based fluids can be viscoelastic. However, comparison of relevant length scales justifies our assumptions of two coexisting fluids with different viscosities. For the dense nanostar phase, the elastic modulus dominates for frequencies larger than ~1 s⁻¹; for shorter frequencies the network is liquid like and the loss modulus dominates²⁹. In comparison, the characteristic active fluid strain rate is $\sigma \approx 5 \times 10^{-3}$ s⁻¹ (Supplementary Fig. 8). Thus, the active fluid deforms the droplet condensates slowly enough to allow for their relaxation, and the droplets behave like viscous fluids. In particular, the viscosity of the droplets is approximately several orders of magnitude higher than water³⁰. Second, our model does not allow to switch off the DNA-MT mechanical coupling and maintains a finite bulk activity as a control for the need of mechanical DNA-MT linkages for the suppression of phase separation. Finally, there are additional mechanisms not considered here that could influence the phase diagram. Also, a large fraction of injected energy in an active fluid is dissipated through channels that do not involve viscous flows⁴⁶. It is possible that such still poorly understood non-viscous dissipation channels could also influence the LLPS phase behaviour.

Conclusions

We merged an active fluid with an equilibrium LLPS to establish an activity-based control of the phase diagram. The stresses induced by the reconfiguring MTs translocate, rupture and dynamically disassemble DNA-based liquid droplets, changing the liquid–liquid coexistence concentrations and suppressing the critical-point temperature. From a fundamental perspective, these results raise intriguing questions about similarities and differences in how internally generated and externally imposed flows affect the equilibrium phase separation. From a materials science perspective, active LLPS provides a foundation for assembling diverse soft active materials. In particular, the coupling between phase separation and activity open

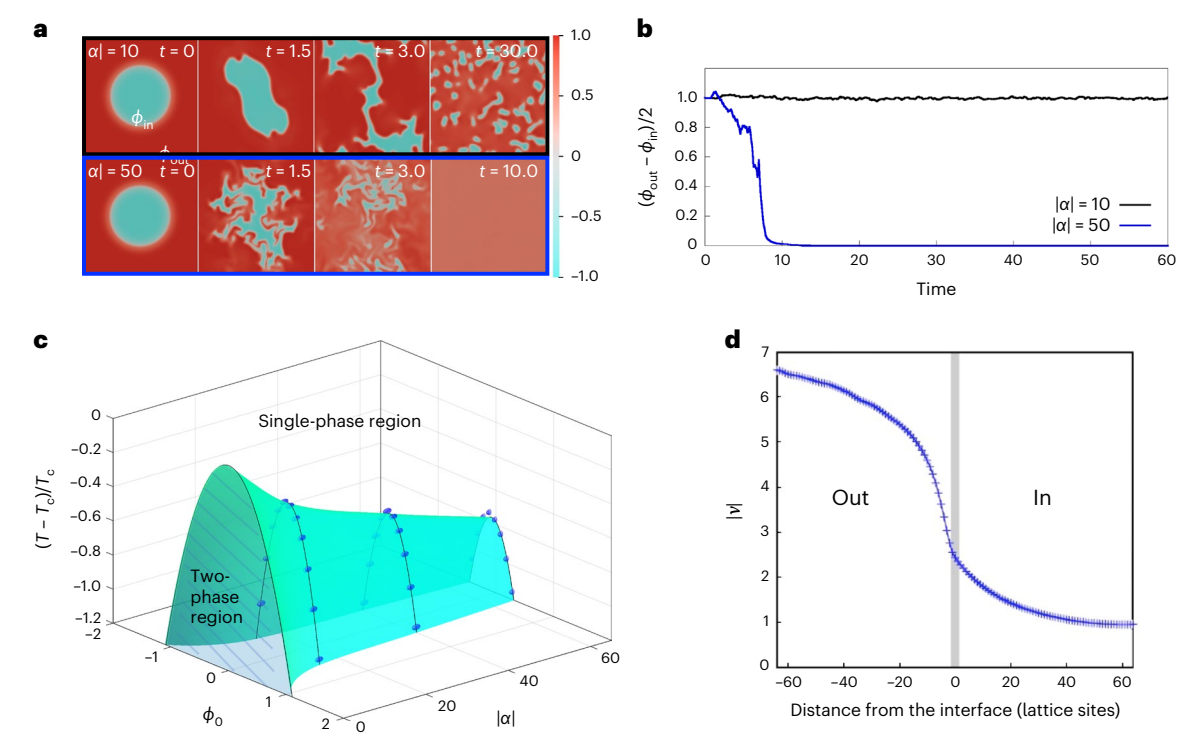


Fig. 6 | **Theoretical model of active LLPS. a**, Simulation time-lapse images for two different activity values: $|\alpha| = 10$ (top), where the activity is arrested but does not suppress phase separation; $|\alpha| = 50$ (bottom), where the activity suppresses phase separation, mixing the system into a homogeneous fluid. Both are below the critical reduced temperature a = -1 of the passive system. **b**, Difference between the coexisting concentrations as a function of time. A value of $\delta \phi = 1$

corresponds to phase separation, whereas $\delta \phi = 0$ corresponds to a uniform state. **c**, Activity-dependent liquid–liquid phase diagram. The curve for $|\alpha| = 0$ is the mean-field coexistence region of the Landau–Ginzburg free energy. The surface is an interpolation between the black curves. **d**, Velocity magnitude, as a function of distance from the interface located at 0. Negative values indicate the position in the dilute phase, and positive values indicate the dense phase.

the path towards creating materials that can incorporate feedback and maintain homoeostasis. Finally, our results are also relevant to cell biology, where phase separation has emerged as an important self-organizing principle^{4,47}. Biological phase separation processes are usually described using thermodynamic formalisms that assume local equilibrium⁴⁸. The cell cytoskeleton, however, is collectively driven away from equilibrium by nanoscale force-generating processes. Our results suggest that active cytoskeletal forces could locally control the spatiotemporal dynamics of membraneless organelles, but this probably requires mechanical coupling between the cytoskeletal network and liquid droplets^{49,50}.

Online content

Any methods, additional references, Nature Portfolio reporting summaries, source data, extended data, supplementary information, acknowledgements, peer review information; details of author contributions and competing interests; and statements of data and code availability are available at https://doi.org/10.1038/s41563-023-01660-8.

References

- Wolde, P. R. T. & Frenkel, D. Enhancement of protein crystal nucleation by critical density fluctuations. Science 277, 1975–1978 (1997).
- van de Witte, P., Dijkstra, P., Van den Berg, J. & Feijen, J. Phase separation processes in polymer solutions in relation to membrane formation. J. Membr. Sci. 117, 1–31 (1996).
- Ianiro, A. et al. Liquid-liquid phase separation during amphiphilic self-assembly. Nat. Chem. 11, 320–328 (2019).
- Brangwynne, C. P. et al. Germline P granules are liquid droplets that localize by controlled dissolution/condensation. Science 324, 1729–1732 (2009).

- Hinze, J. O. Fundamentals of the hydrodynamic mechanism of splitting in dispersion processes. AIChE J. 1, 289–295 (1955).
- Onuki, A. Phase transitions of fluids in shear flow. J. Phys. Condens. Matter 9, 6119 (1997).
- Berthier, L. Phase separation in a homogeneous shear flow: morphology, growth laws, and dynamic scaling. *Phys. Rev. E* 63, 051503 (2001).
- Han, C. C., Yao, Y., Zhang, R. & Hobbie, E. K. Effect of shear flow on multi-component polymer mixtures. *Polymer* 47, 3271–3286 (2006).
- 9. Olmsted, P. D. Perspectives on shear banding in complex fluids. *Rheol. Acta* **47**, 283–300 (2008).
- Zhang, R. et al. Phase separation mechanism of polybutadiene/ polyisoprene blends under oscillatory shear flow. Macromolecules 41, 6818–6829 (2008).
- Pine, D., Easwar, N., Maher, J. V. & Goldburg, W. Turbulent suppression of spinodal decomposition. *Phys. Rev. A* 29, 308 (1984).
- 12. Marchetti, M. C. et al. Hydrodynamics of soft active matter. Rev. Mod. Phys. **85**, 1143 (2013).
- Nakashima, K. K., van Haren, M. H., André, A. A., Robu, I. & Spruijt,
 E. Active coacervate droplets are protocells that grow and resist
 Ostwald ripening. Nat. Commun. 12, 3819 (2021).
- Nguyen, N. H., Klotsa, D., Engel, M. & Glotzer, S. C. Emergent collective phenomena in a mixture of hard shapes through active rotation. *Phys. Rev. Lett.* 112, 075701 (2014).
- Soni, V. et al. The odd free surface flows of a colloidal chiral fluid. Nat. Phys. 15, 1188–1194 (2019).
- Testa, A. et al. Sustained enzymatic activity and flow in crowded protein droplets. Nat. Commun. 12, 6293 (2021).

- Adkins, R. et al. Dynamics of active liquid interfaces. Science 377, 768–772 (2022).
- Theurkauff, I., Cottin-Bizonne, C., Palacci, J., Ybert, C. & Bocquet, L. Dynamic clustering in active colloidal suspensions with chemical signaling. *Phys. Rev. Lett.* 108, 268303 (2012)
- Palacci, J., Sacanna, S., Steinberg, A. P., Pine, D. J. & Chaikin, P. M. Living crystals of light-activated colloidal surfers. *Science* 339, 936–940 (2013).
- Redner, G. S., Hagan, M. F. & Baskaran, A. Structure and dynamics of a phase-separating active colloidal fluid. *Phys. Rev. Lett.* 110, 055701 (2013).
- Zhang, J., Alert, R., Yan, J., Wingreen, N. S. & Granick, S. Active phase separation by turning towards regions of higher density. *Nat. Phys.* 17, 961–967 (2021).
- Fily, Y. & Marchetti, M. C. Athermal phase separation of self-propelled particles with no alignment. *Phys. Rev. Lett.* 108, 235702 (2012)
- Redner, G. S., Baskaran, A. & Hagan, M. F. Reentrant phase behavior in active colloids with attraction. *Phys. Rev. E* 88, 012305 (2013).
- Schwarz-Linek, J. et al. Phase separation and rotor self-assembly in active particle suspensions. *Proc. Natl Acad. Sci. USA* 109, 4052–4057 (2012).
- Ross, T. D. et al. Controlling organization and forces in active matter through optically defined boundaries. *Nature* 572, 224–229 (2019).
- Banani, S. F., Lee, H. O., Hyman, A. A. & Rosen, M. K. Biomolecular condensates: organizers of cellular biochemistry. *Nat. Rev. Mol. Cell Biol.* 18, 285–298 (2017).
- Biffi, S. et al. Phase behavior and critical activated dynamics of limited-valence DNA nanostars. Proc. Natl Acad. Sci. USA 110, 15633–15637 (2013).
- Sanchez, T., Chen, D. T., DeCamp, S. J., Heymann, M. & Dogic, Z. Spontaneous motion in hierarchically assembled active matter. Nature 491, 431–434 (2012).
- Conrad, N., Kennedy, T., Fygenson, D. K. & Saleh, O. A. Increasing valence pushes DNA nanostar networks to the isostatic point. Proc. Natl Acad. Sci. USA 116, 7238–7243 (2019).
- Jeon, B.-j et al. Salt-dependent properties of a coacervate-like, self-assembled DNA liquid. Soft Matter 14, 7009–7015 (2018).
- Nguyen, D. T., Jeon, B.-j, Abraham, G. R. & Saleh, O. A. Length-dependence and spatial structure of DNA partitioning into a DNA liquid. *Langmuir* 35, 14849–14854 (2019).
- Tayar, A. M., Hagan, M. F. & Dogic, Z. Active liquid crystals powered by force-sensing DNA-motor clusters. *Proc. Natl Acad.* Sci. USA 118, e2102873118 (2021).
- Hilitski, F. et al. Measuring cohesion between macromolecular filaments one pair at a time: depletion-induced microtubule bundling. *Phys. Rev. Lett.* 114, 138102 (2015).
- Andre, A. A. M., Yewdall, N. A. & Spruijt, E. Crowding-induced phase separation and gelling by co-condensation of PEG in NPM1-rRNA condensates. *Biophys. J.* 122, 397–407 (2023).

- Bate, T. E., Jarvis, E. J., Varney, M. E. & Wu, K.-T. Collective dynamics of microtubule-based 3D active fluids from single microtubules. Soft Matter 15, 5006–5016 (2019).
- Singh, R. & Cates, M. Hydrodynamically interrupted droplet growth in scalar active matter. *Phys. Rev. Lett.* 123, 148005 (2019).
- Tiribocchi, A., Wittkowski, R., Marenduzzo, D. & Cates, M. E. Active model H: scalar active matter in a momentum-conserving fluid. *Phys. Rev. Lett.* 115, 188302 (2015)
- Chandrakar, P. et al. Confinement controls the bend instability of three-dimensional active liquid crystals. *Phys. Rev. Lett.* 125, 257801 (2020).
- Thampi, S. P., Golestanian, R. & Yeomans, J. M. Velocity correlations in an active nematic. *Phys. Rev. Lett.* 111, 118101 (2013).
- 40. Blow, M. L., Thampi, S. P. & Yeomans, J. M. Biphasic, lyotropic, active nematics. *Phys. Rev. Lett.* **113**, 248303 (2014).
- 41. Giomi, L. & DeSimone, A. Spontaneous division and motility in active nematic droplets. *Phys. Rev. Lett.* **112**, 147802 (2014).
- 42. Hughes, R. & Yeomans, J. M. Collective chemotaxis of active nematic droplets. *Phys. Rev. E* **102**, 020601 (2020).
- 43. Marenduzzo, D., Orlandini, E., Cates, M. & Yeomans, J. Steadystate hydrodynamic instabilities of active liquid crystals: hybrid lattice Boltzmann simulations. *Phys. Rev. E* **76**, 031921 (2007).
- 44. Simha, R. A. & Ramaswamy, S. Hydrodynamic fluctuations and instabilities in ordered suspensions of self-propelled particles. *Phys. Rev. Lett.* **89**, 058101 (2002).
- 45. Cates, M. E. in Active Matter and Nonequilibrium Statistical Physics: Lecture Notes of the Les Houches Summer School Vol. 112 (eds Gompper, G., Cristina Marchetti, M., Tailleur, J. & Yeomans, J. M.) (Oxford Univ. Press, 2019).
- Foster, P. J. et al. Dissipation and energy propagation across scales in an active cytoskeletal material. *Proc. Natl Acad. Sci. USA* 120, e2207662120 (2023).
- Shin, Y. & Brangwynne, C. P. Liquid phase condensation in cell physiology and disease. Science 357, eaaf4382 (2017)
- 48. Fritsch, A. W. et al. Local thermodynamics govern formation and dissolution of *Caenorhabditis elegans* P granule condensates. *Proc. Natl Acad. Sci. USA* **118**, e2102772118 (2021).
- Setru, S. U. et al. A hydrodynamic instability drives protein droplet formation on microtubules to nucleate branches. *Nat. Phys.* 17, 493-498 (2021).
- Wiegand, T. & Hyman, A. A. Drops and fibers—how biomolecular condensates and cytoskeletal filaments influence each other. *Emerg. Top. Life Sci.* 4, 247–261 (2020).

Publisher's note Springer Nature remains neutral with regard to jurisdictional claims in published maps and institutional affiliations.

Springer Nature or its licensor (e.g. a society or other partner) holds exclusive rights to this article under a publishing agreement with the author(s) or other rightsholder(s); author self-archiving of the accepted manuscript version of this article is solely governed by the terms of such publishing agreement and applicable law.

@ The Author(s), under exclusive licence to Springer Nature Limited 2023

Methods

Tubulin purification and MT polymerization

Tubulin was purified from bovine brain through two cycles of polymerization and depolymerization 51 . Tubulin was stored at $-80\,^{\circ}\text{C}$ and recycled through an additional cycle of polymerization and depolymerization. Tubulin was labelled with Alexa Fluor 647 dye for fluorescent imaging using a succinimidyl ester linker 52 . Recycled and labelled tubulin was flash frozen in liquid nitrogen and stored at $-80\,^{\circ}\text{C}$. MTs were polymerized at $8\,\text{mg ml}^{-1}$ tubulin concentration in M2B buffer (80 mM PIPES at pH 7.0, 1 mM EGTA, 2 mM MgCl $_2$) containing 20 mM DTT and 10 mM GMPCPP (Jena Bioscience), a non-hydrolysable analogue of GTP. The mixture was incubated on ice for 10 min, subsequently at 37 $^{\circ}\text{C}$ for 30 min and allowed to sit at room temperature for 3 h, flash frozen in liquid nitrogen and stored at $-80\,^{\circ}\text{C}$. Fluorescent MTs contained 5% Alexa Fluor 647-labelled tubulin.

Kinesin purification

Dimeric kinesin, consisting of 401 amino acids of the N-terminal motor domain of Drosophila melanogaster kinesin-1 fused to the SNAP-tag, was purified as previously described 28,53 . The SNAP-tag is appended to the cargo-binding region of the motor. The protein was flash frozen in liquid nitrogen and stored at -80 °C.

Modifying DNA oligos

5′-Amine-modified DNA oligos (Integrated DNA Technologies) were labelled with BG-GLA-NHS (New England Biolabs) 32,54,55 . Briefly, BG-GLA-NHS was dissolved in dimethyl sulfoxide to a final concentration of 20 mM. Amine-modified DNA oligos were dissolved at 2 mM in HEPES buffer (150 mM, pH 8.4). BG-GLA-NHS solution was added to DNA oligos at a final BG concentration of 7 μ M. The mixture was incubated for 30 min at room temperature. DNA was separated from excess BG using a size-exclusion spin column (Micro Bio-Spin 6 columns, Bio-Rad). Before DNA cleaning, Tris buffer in the column was exchanged with phosphate-buffered saline (0.2×) (pH7.2) according to the manufacturer's instructions. The separation step was repeated four times. DNA oligos were concentrated using a SpeedVac to a final concentration of 5–10 μ g μ l-1.

Assembling DNA nanostars

Four-armed DNA nanostars were assembled from four distinct 49-base-pair-long DNA oligos 30 , with 6-base-pair sticky palindromic overhang AGGCCT, and one unpaired base (Supplementary Fig. 1). DNA oligos were mixed at an equal concentration of $20~\mu g~\mu l^{-1}$ in TAE buffer (40 mM Tris, 20 mM acetic acid, 1 mM EDTA, pH 8.2) and 25% of sequence 1 was labelled with a BG modification. DNA oligos were annealed to their complementary strands. DNA was heated to 95 °C for 10 min and gradually cooled down to room temperature in a heat block left on the bench. DNA nanostars were stored at $-20~\rm ^{\circ}C$.

DNA nanostar oligos sequence

Sequence 1: AGGCCTAGCTCAACGGTGAGTTGCACGTTCGGC CGTTCCCAGAGAAAGC

Sequence 1 (for modifications): AGCTCAACGGTGAGTTGC ACGTTCGGCCGTTCCCAGAGAAAGC

Sequence 2: AGGCCTAGCGTCAAACCACACTCGCACTTCGTGCAACTCACCGTTGAGC

Sequence 3: -AGGCCTAGCCGCCGCCGCATCGCCCGCTTGTGCGAGTGTGGTTTGACGC

Sequence 4: -AGGCCTTGCTTTCTCTGGGAACGGCCGTTGCGGGCGATGCGGCGGCGGC

DNA nanostars have 98 base pairs and their molecular weight is $-65,000\,\mathrm{Da}$.

Active gel mixture

The final active mixture contained a varying concentration of kinesin–DNA complexes in the range of $0-5.5 \,\mu\text{M}$, as indicated in the figures

in the main text. DNA nanostar mixtures contained 25% BG-labelled nanostars and 75% four-arm nanostars (Supplementary Fig. 1). DNA nanostar concentration was either 40 μM (2.5 mg ml $^{-1}$) or 70 μM (4.5 mg ml $^{-1}$), as indicated in the figures in the main text. All the other components were dissolved in M2B buffer (80 mM PIPES, 2 mM MgCl $_2$, 1 mM EGTA, pH 6.8 using KOH) and had fixed concentrations. These included the following: (1) MT final concentration of 1.10 mg ml $^{-1}$ (-10 μM); (2) 2% w/v PEG at 35 kDa; (3) 26.6 mM phosphoenolpyruvic acid; (4) 1.4 mM ATP; (5) 6.70 mg ml $^{-1}$ glucose; (6) 0.40 mg ml $^{-1}$ glucose oxidase; (7) 0.08 mg ml $^{-1}$ glucose catalase; (8) 5.0 mM DTT; (9) pyruvate kinase/lactic dehydrogenase, 0.03 U ml $^{-1}$.

The final sample was assembled in the following steps:

- Active mixture 1: the samples contained an ATP regeneration and antioxidant mixture that ensured steady-state kinesin stepping speed and minimizing photobleaching effects. The final sample contained 26.6 mM phosphoenolpyruvic acid, 1.4 mM ATP, 6.70 mg ml⁻¹ glucose, 0.40 mg ml⁻¹ glucose oxidase, 0.08 mg ml⁻¹ glucose catalase, 2.0 mM MgCl₂, 5.0 mM DTT and pyruvate kinase/lactic dehydrogenase²⁸. This solution can be stored concentrated 2.5× at -80 °C and used on the day of the experiment.
- Active mixture 2: antioxidants and depletant—to form the active nanostars, a mixture was prepared as follows: 10 μl ATP regeneration system (active mixture 1), 8 μl M2B buffer, 5 μl PEG (35 kDa, 12% w/v) were mixed at room temperature.
- 3. Active mixture 3: binding DNA nanostars to kinesin motors—the DNA nanostar mixture was thawed at 45 °C for 5 min and cooled down to room temperature. The nanostar mixture was added at equal volume to active mixture 2 and incubated for 2 h at 15 °C. Kinesin motor stock was added to the mixture at the desired concentration (as specified in the main text) and mixed using a pipette with a wide tip. The mixture was incubated at 15 °C for 1 h. Previous work estimated the efficiency of kinesin–DNA binding at 70–80% (ref. 34).
- 4. Assembling the active gel: to assemble an active gel, 5μ l of active mixture 2 was added to 5μ l of active mixture 3 and 2μ l of polymerized MTs at $6.8 \, \text{mg ml}^{-1}$.
- 5. Flow and data acquisition protocol: the final active gel was placed into a parafilm chamber sandwiched between two acrylamide-coated coverslips⁵². The capillary dimensions were $0.12 \times 2.00 \times 20.00 \text{ mm}^3$. The chamber was then sealed with Norland adhesive glue, and cured with ultraviolet light. The samples were immediately taken to the microscope after assembly, and observations started a couple of minutes after the activity was initiated.

Fluorescent labelling of kinesin

SNAP-tagged kinesin motors were mixed with BG-Alexa Fluor 488 (New England Biolabs), at a ratio of 10:1, in M2B buffer containing 0.5 μM DTT. The mixture was incubated for 30 min at room temperature and sequentially added to the BG-labelled DNA nanostars.

Optical microscopy imaging

For imaging and quantifying the total DNA concentration, we used YOYO-1 intercalating dye at a concentration of 100–200 nM. For measuring the tielines, DNA nanostars were internally labelled with Cy5 fluorophore at the core of the nanostar. Active gels were imaged using conventional fluorescence microscopy with Nikon Ti2 and an Andor Zyla 5.5 camera running open-source microscopy managing software Micro-Manager 1.4.23. Three-dimensional volumes and droplet deformation profiles were extracted from the confocal images acquired with Nikon ECLIPSE Ti2 having CrestOptics confocal X-light V2 and a Photometrics 95B camera. The experiments were conducted on a Tokai HIT CBU thermal plate operating in the range of 10–55 °C. The

fluorescence correlation spectroscopy measurements were conducted on a Leica SP8 confocal scanning laser microscope, with a Plan Apo 63×/1.2-numerical-aperture water-immersion lens and the Leica fluorescence correlation spectroscopy module.

Measuring DNA concentrations between coexisting phases

Partitioning of DNA between the dilute and dense phases was calculated from the fluorescent intensity and the two-dimensional area fraction of each phase. Since the droplet diameter is typically larger than the chamber height of 120 µm, the active LLPS was treated as a quasi-two-dimensional sample: therefore, the ratio of the area fraction indicates the ratio of the volume fractions. To measure the intensity of the entire volume section, we used a 2×/0.1-numerical-aperture objective with a 100 um depth of field. Close to the binodal curve. the droplet diameters were smaller than the channel depth; therefore, the area-volume fraction of smaller droplets was overestimated. Each measurement was kept at a constant temperature until the ATP was depleted. For the active LLPS, the concentrations were extracted from the steady-state values of each phase concentration about an hour before the ATP depletion (Supplementary Fig. 3). For the passive regimes, the measurements were taken after the droplets relaxed to their final shape at about t = 10-15 h.

DNA cluster size in the dilute phase

We characterized the structure of the dilute phase using fluorescence correlation spectroscopy. The fluorescence intensity fluctuations due to Brownian motion reveal the distribution of diffusion times and consequently the size of nanostar clusters. Fluorescent correlation spectroscopy measurements were conducted in the dilute DNA phase for kinesin-decorated DNA droplets and for passive DNA droplets.

Projection of MTs on DNA droplets

To quantify the interactions between DNA and MTs, 3D confocal images were acquired. The evolving surface of the droplets was extracted from the 3D volume images using the TubULAR toolkit, with an MT projection at a distance of 5–11 μm from the surface 56 .

Data availability

All data supporting the findings of this study are available within the Article and its Supplementary Information. Source data are provided with this paper.

Code availability

The numerical code used to generate the thermotical phase diagram is available via GitHub at https://github.com/fcaballerop/nematicPhaseFieldFoam.

References

51. Castoldi, M. & Popova, A. V. Purification of brain tubulin through two cycles of polymerization-depolymerization in a high-molarity buffer. *Protein Expr. Purif.* **32**, 83–88 (2003).

- Tayar, A. M., Lemma, L. M. & Dogic, Z. Assembling microtubule-based active matter. *Methods Mol. Biol.* 2430, 151–183 (2022).
- 53. Young, E. C., Berliner, E., Mahtani, H. K., Perezramirez, B. & Gelles, J. Subunit interactions in dimeric kinesin heavy-chain derivated that lack the kinesin rod. *J. Biol. Chem.* **270**, 3926–3931 (1995).
- 54. Derr, N. D. et al. Tug-of-war in motor protein ensembles revealed with a programmable DNA origami scaffold. Science **338**, 662–665 (2012).
- Goodman, B. S. & Reck-Peterson, S. L. in Reconstituting the Cytoskeleton Methods in Enzymology (ed Vale, R. D.) Vol. 540, 169–188 (2014).
- 56. Mitchell, N. P. & Cislo, D. J. TubULAR: tracking *in toto* deformations of dynamic tissues via constrained maps. Preprint at *bioRxiv* https://doi.org/10.1101/2022.04.19.488840 (2022).

Acknowledgements

We thank P. Gulati, Z. You, G. Abraham and S. Takatori for fruitful discussions. We thank N. Mitchell for help with the analysis of the 3D images. This work was primarily supported by the US Department of Energy, Basic Energy Sciences, through award DE-SC001973. The initial stages of the theoretical modelling were supported by NSF-DMR-2041459. We also acknowledge the use of the Brandeis MRSEC Bio-Synthesis Facility, which is supported by NSF-MRSEC-2011846. O.A.S. acknowledges support from the W.M. Keck Foundation. A.M.T. is a Simons Foundation Fellow of the Life Sciences Research Foundation and is an Awardee of the Weizmann Institute of Science–National Postdoctoral Award Program for Advancing Women in Science.

Author contributions

A.M.T., O.A.S. and Z.D. designed the experiments. A.M.T. performed the experimental work and data analysis. T.A. helped with the data analysis. F.C. and M.C.M. developed the theory. A.M.T., M.C.M. and Z.D. wrote the manuscript. All authors edited the manuscript.

Competing interests

The authors declare no competing interests.

Additional information

Supplementary information The online version contains supplementary material available at https://doi.org/10.1038/s41563-023-01660-8.

Correspondence and requests for materials should be addressed to Alexandra M. Tayar or Zvonimir Dogic.

Peer review information *Nature Materials* thanks Steve Granick for his contribution to the peer review of this work.

Reprints and permissions information is available at www.nature.com/reprints.